JACS
JOURNAL OF THE AMERICAN CHEMICAL SOCIETY
Article
pubs.acs.org/JACS

Bridging the Gap: Electron Relay and Plasmonic Sensitization of Metal Nanocrystals for Metal Clusters

Fang-Xing Xiao, Zhiping Zeng, and Bin Liu*

School of Chemical and Biomedical Engineering, Nanyang Technological University, 62 Nanyang Drive, Singapore 637459, Singapore

Supporting Information

ABSTRACT: In recent years, enormous attention has been paid to the construction of metal cluster-semiconductor nanocomposites because of the fascinating and unique properties of metal clusters; however, investigations on photoelectrochemical (PEC) and photocatalytic properties of metal cluster-semiconductor systems are still rare. Moreover, to date, intrinsic correlation between metal clusters and bulk metal nanocrystals has yet to be elucidated. In this work, a facile layer-by-layer (LbL) self-assembly strategy has been developed to judiciously and intimately integrate gold nanocrystals (Au) within the interface between gold clusters (Au_x) and hierarchically ordered TiO_2 nanotube arrays framework, by which imperative roles of Au nanocrystals as electron relay mediator and plasmonic sensitizer for Au_x clusters were revealed. In addition, it was found that synergistic interaction between Au nanocrystals and Au_x clusters contributed to promising visible-light-driven photocatalytical and PEC performances. It is anticipated that our work could provide a general way for rationally constructing metal and metal clusters codecorated semiconductor heterostructures and, more significantly, bridge the gap between metal clusters and metal nanocrystals for a diverse range of applications.

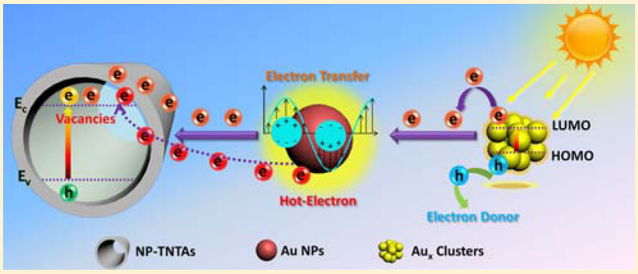

1. INTRODUCTION

One-dimensional (1D) semiconductor nanostructures have ignited massive research interests in the past decade for a diverse range of applications due to their unique structural and electronic properties such as fast electron transport, large specific surface area, and orthogonalized light absorption and minority carrier diffusion.[1,2] Among which, 1D TiO_2-based nanostructures feature a high degree of vertically oriented geometry and unidirectional charge transfer channel, thereby making them prime candidates for photocatalytic and photoelectrochemical (PEC) applications.[3,4] Nonetheless, poor light absorption in visible light spectrum and fast recombination of photoexcited electron−hole charge carriers remarkably hinder the potential applications of TiO_2.[5] To overpass these obstacles, various synthetic strategies have thus been explored including metal or nonmetal doping,[6,7] metal deposition,[8,9] and heterocoupling with narrow-band gap semiconductors.[10,11] Despite these endeavors, seeking for new 1D TiO_2-based light-harvesting systems still constitutes a central challenge.

Metal nanoparticles (NPs) represent an important sector of nanomaterials due to their unique plasmonic effect.[12−16] Most significantly, plasmon excitation can trigger a coherent oscillation of electrons in NPs, producing a strong electromagnetic field that is beneficial for enhancing optical transition in neighboring molecules and/or semiconductors and hence boosting the quantum yield of photochemical reactions.[17,18] When the size of metal NPs becomes atomically small (<2 nm), with precise number of metal atoms and protected by a stabilizing ligand, they are referred to as "metal clusters".[19−25] Contrary to metal NPs, metal clusters are featured by peculiar atom packing, effect of quantum confinement, and discrete molecule-like band structure. Albeit the progresses, up to date, it is still unclear the specific interaction between these two optically different metal NPs/clusters and their specific contributing roles under light illumination. Moreover, inspired by inherent merits of metal NPs and clusters, two questions are naturally raised: whether the optical/electronic interaction between clusters and NPs would affect the overall photoactivities of metal nanostructures, and whether the plasmon excitation of meal NPs, photosensitization of metal clusters, and structural advantages of 1D large bandgap semiconductors (e.g., TiO_2) could be judiciously integrated within a ternary system for substantial light harvesting especially in the visible light spectrum?

On the other hand, in recent years, explosive studies regarding the construction of metal nanostructures/semiconductor nanocomposites have been reported; nevertheless, most of the synthetic strategies are predominantly based on conventional approaches including hydrothermal synthesis, sol−gel, dipping/calcination, photodeposition, and deposition/precipitation, which not only require complicated and delicate processes, but also are difficult to integrate the components at nanoscale.[26] On the contrary, layer-by-layer

Received: June 18, 2015
Published: August 10, 2015

DOI: 10.1021/jacs.5b06323
J. Am. Chem. Soc. 2015, 137, 10735−10744

(LbL) self-assembly technique, as a prominent bottom-up strategy, demonstrates tremendous merits in comparison with conventional approaches in terms of the versatility and simplicity, which is beneficial for delicate control over the thickness, structure, and component of the multilayered thin films or nanostructures at molecular-level.[27−30] Therefore, it is highly desirable to construct a well-defined ternary system in which metal nanocrystals and metal clusters could be intimately LbL assembled on the scaffold of 1D semiconductors (e.g., TiO_2).

With these motivations, in this work, a facile and green LbL self-assembly approach has been developed to couple Au NPs and glutathione (GSH)-capped Au_x clusters with nanoporous TiO_2 nanotube arrays (NP-TNTAs) in a tunable fashion. More significantly, the imperative roles of Au NPs as electron relay mediator and plasmonic sensitizer for Au_x clusters were for the first time clearly ascertained. In addition, it was found that the synergistic interaction between Au NPs and Au_x clusters contributed significantly to the enhanced PEC and photocatalytic performances of ternary nanostructures. It is anticipated that our work could provide new insights for different sized Au nanostructures to bridge the gap between metal nanocrystals and metal clusters for a diverse range of potential applications.

2. EXPERIMENTAL SECTION

2.1. Materials. Titanium sheets (99.9%), deionized water (DI H_2O, Milipore, 18.2 MΩ·cm), graphite sheet (99.6%), ethylene glycol $(CH_2OH)_2$, ammonium fluoride (NH_4F), hydrogen fluoride (HF), nitric acid (HNO_3), hydrochloric acid (HCl), L-glutathione (reduced, 98%), gold(III) chloride trihydrate (99.9%), sodium citrate, sodium chloride (NaCl), poly(diallyldimethylammonium chloride) (PDDA; 1 mg/mL, 0.5 M NaCl, $M_w \approx 200\,000-350\,000$), 3-aminopropyltrimethoxysilane (APS), 4-nitroaniline (4-NA), 3-NA, 2-NA, 4-nitrophenol (4-NP), 3-NP, 2-NP, ammonium formate (NH_4HCO_2), and potassium persulfate ($K_2S_2O_8$).

2.2. Synthesis of L-Glutathione Capped Au_x Clusters. The synthesis of Au_x clusters followed previous work.[19−21] Briefly, gold(III) chloride trihydrate (40 mg) and L-glutathione (GSH, 46 mg) were thoroughly mixed in 50 mL of DI H_2O at ambient conditions. The mixture was continuously stirred until the appearance of a colorless solution and then was heated at 70 °C for 24 h. Subsequently, acetonitrile was added to the cluster solution to purify the clusters followed by washing several times with mixed solution of DI H_2O and acetonitrile (1:3 in volume). Finally, the clusters were redissolved in DI H_2O and stored at ambient conditions.

2.3. Preparation of Au NPs. The synthesis of Au NPs capped with negatively charged citrate ions was adopted from a previous method.[31] Prior to experiment, all glassware were cleaned thoroughly with aqua regia (3:1 in volume for HCl and HNO_3) for 12 h and thoroughly washed with DI H_2O. Gold(III) chloride (25 mL, 1 mM) and sodium citrate (2.5 mL, 38.8 mM) aqueous solutions were separately heated to boil under vigorous stirring. Subsequently, the latter was rapidly added into the gold solution under vigorous stirring (1200 rpm). The mixture became dark and then wine red gradually in 20 s, and the heating was lasted for 10 min. Finally, the solution was vigorously stirred under ambient conditions for another 15 min to finish the synthetic process.

2.4. Fabrication of Hierarchically Ordered NP-TNTAs Substrate. Ti foil was first sonicated in acetone, ethanol and DI H_2O, respectively. Subsequently, the cleaned Ti foil was treated with HF−HNO_3−H_2O mixed solution (1:4:5 in volume) for 30 s, thoroughly washed by DI H_2O and dried with N_2. Anodization was performed under ambient conditions (50 V, 2 h) to prepare TNTAs, in which Ti foil and graphite sheet were used as the working electrode and counter electrode, respectively. The electrolyte consisted of 0.3 wt % NH_4F, ethylene glycol (196 mL) and DI H_2O (4 mL). The resultant TNTAs were thoroughly washed by DI H_2O, dried with a gentle stream of N_2, and vigorously sonicated in ethanol or DI H_2O to remove the surface layer. Anodization was repeated again (50 V, 30 min) to prepare the NP-TNTAs. In a similar way, NP-TNTAs were subjected to the same washing and drying procedures and finally calcined in air (450 °C, 1 h, 2 °C/min). TiO_2 thin film counterpart was prepared by vigorously sonicating the anodized NP-TNTAs in ethanol (25 min) and calcined under the same experimental conditions.

2.5. Fabrication of Au_x/NP-TNTAs and Au/NP-TNTAs Binary Heterostructures. NP-TNTAs (30 mm × 10 mm) was immersed in an acid solution (HCl, 1 M) for 30 min, thoroughly cleaned by DI H_2O and dried with a gentle stream of N_2. Afterward, the acid-treated NP-TNTAs was immersed into Au_x clusters solution at ambient conditions for 48 or 125 h, followed by the same washing and drying procedures, which produced Au_x/NP-TNTAs binary nanostructure. For the fabrication of Au/NP-TNTAs nanostructure, NP-TNTAs was dipped into PDDA (1 mg/mL, 0.5 M NaCl, pH = 8) aqueous solution for 20 min, washed with DI H_2O, followed by drying with a N_2 stream. Afterward, the PDDA-modified NP-TNTAs was immersed into citrate-stabilized Au NPs aqueous solution for 20 min. Finally, the thus-obtained Au/NP-TNTAs nanostructure was calcined at 450 °C in air for 1 h to remove PDDA, giving rise to Au/NP-TNTAs binary heterostructure. The deposition amount of Au NPs in Au/NP-TNTAs was tuned by varying assembly cycles via analogous assembly process.

2.6. Preparation of Au_x/Au/NP-TNTAs Ternary Heterostructures. The calcined Au/NP-TNTAs nanostructure was first subjected to plasma treatment and then rapidly dipped into APS solution (1% volume in ethanol) for 1 h, thoroughly washed with ethanol for three times and dried with a gentle N_2 stream. Following, the APS-modified Au/NP-TNTAs was immersed into Au_x clusters solution for different periods of time under ambient conditions, washed with DI H_2O, and dried with a N_2 stream. Noteworthily, when dipping time is longer than 48 h, the samples were withdrawn regularly from Au_x clusters solution every 24 h, washed with DI H_2O, dried with N_2, and then dipped into APS solution for 30 min. After the same washing and drying procedures, the samples were reimmersed into Au_x clusters aqueous solution again until the desired dipping time. Finally, the composites were irradiated with weak UV light (365 ± 15 nm) for 60 min to remove APS, resulting in Au_x/Au/NP-TNTAs ternary heterostructures. To construct Au/Au_x/NP-TNTAs nanostructure with reversed deposition sequence of Au NPs and Au_x clusters to Au_x/Au/NP-TNTAs, Au_x/NP-TNTAs nanostructure was dipped into the same PDDA solution for 20 min, and subjected to the same washing and drying procedures. Afterward, the PDDA-modified Au_x/NP-TNTAs was immersed into citrate-capped Au NPs aqueous solution for 20 min and subjected to the same washing and drying processes. Finally, the composite was calcined at 450 °C in argon for 1 h leading to Au/Au_x/NP-TNTAs nanostructure.

2.7. Characterization. Crystal structure was studied by X-ray diffraction (Bruker D8, 40 kV, 40 mA) using Cu Kα as the radiation source. Transmission electron microscopy (TEM) and high-resolution (HR) TEM images were collected by a JEOL model JEM 2010 EX instrument (200 kV). UV−vis diffuse reflectance spectra (DRS) were obtained on a UV−vis-NIR spectrometer (Varian Cary 500 Scan) using $BaSO_4$ as the background. X-ray photoelectron spectroscopy (XPS) spectra were collected on a photoelectron spectrometer (ESCALAB 250, Thermo Fisher Scientific), binding energy (BE) of the element was calibrated based on the BE of carbon (284.60 eV). Morphology was probed by field emission scanning electron microscopy (FESEM, JEOL JSM6701F). Fourier transform infrared (FTIR) spectra were recorded on a PerkinElmer FTIR spectrometer. Photoluminescence (PL) spectra were collected by an LP920-KS instrument. Quantitative cathodoluminescence was measured on an Attolight Rosa 4634 microscope, in which a high-speed achromatic reflective lens (N.A. 0.72) was tightly integrated within the objective lens of a field emission gun scanning electron microscope (FEG-SEM) and electron beam energies of 8 kV with dwell time of 0.2 s were used to excite the samples. Atomic force microscopy (AFM, MFP3D, Asylum Research) images were taken by a silicon cantilever, which

DOI: 10.1021/jacs.5b06323
J. Am. Chem. Soc. 2015, 137, 10735−10744

Scheme 1. LbL Assembly of Hierarchically Ordered Au_x/Au/NP-TNTAs Ternary Heterostructure

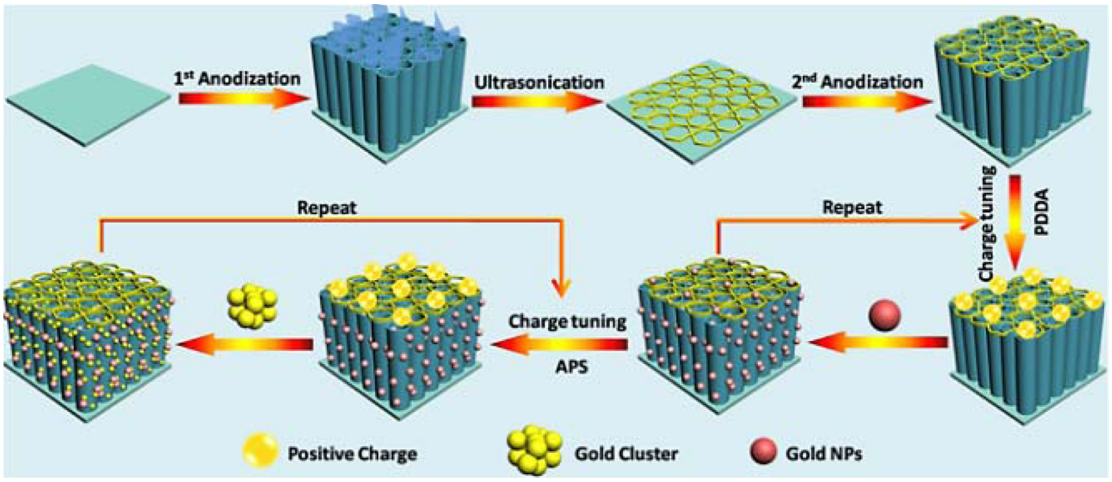

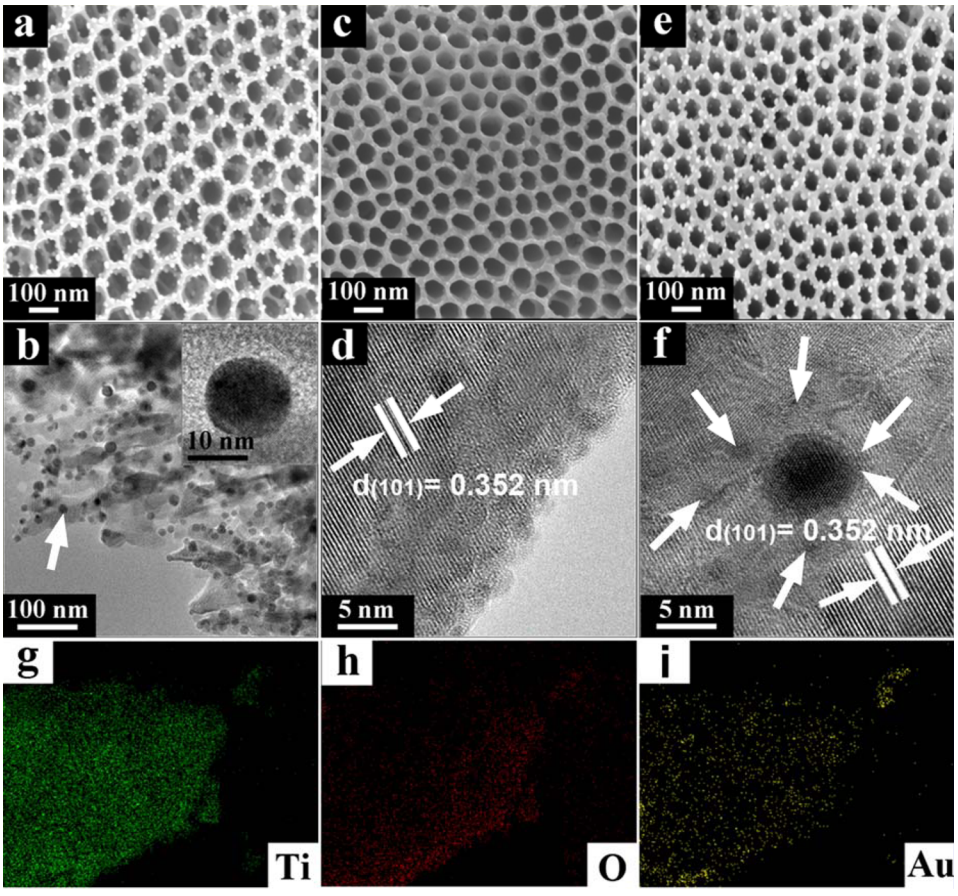

Figure 1. FESEM and TEM images of (a and b) Au/NP-TNTAs, (c and d) Au_x/NP-TNTAs, and (e and f) Au_x/Au/NP-TNTAs. Elemental mapping results of Au_x/Au/NP-TNTAs show (g) Ti, (h) O, and (i) Au signals.

operates in a tapping mode. Dynamic light scattering analysis (Zeta PALS, Brookhaven Instruments Co.) was used to determine the Zeta potential. Raman spectra were collected on a RenishawinVia Raman System 1000 using an excitation source of 514 nm under ambient conditions.

2.8. Photoelectrochemical (PEC) Measurements. PEC measurements were performed on an electrochemical workstation (CHI 660D). The electrochemical setup is composed of conventional three-electrodes, a quartz cell containing 20 mL Na_2S (0.1 M) aqueous solution and a potentiostat. A platinum plate (20 mm × 10 mm) was used as counter electrode and Hg/HgCl/KCl as reference electrode. The sample films (20 mm × 10 mm) were vertically dipped into electrolyte and irradiated with a 300 W xenon arc lamp (Newport) equipped with a UV cutoff filter (λ > 420 nm) and an AM 1.5 filter. Monochromatic incident photon-to-electron conversion efficiency (IPCE) spectra were collected using three-electrode without bias, for which monochromatic light was provided by a 300 W xenon arc lamp (Newport) combined with a monochromator (Newport).

2.9. Photocatalytic Performances. The sample films were vertically dipped into 2.5 mL nitro compounds (5 mg. L^{-1}) in a sealed quartz vial reactor, which was added with HCO_2NH_4 (40 mg). The experiments were carried out with N_2 bubbling under ambient

DOI: 10.1021/jacs.5b06323
J. Am. Chem. Soc. 2015, 137, 10735−10744

conditions. A 300 W xenon arc lamp (Newport) equipped with a UV cutoff filter (λ > 420 nm) served as light source for visible light irradiation. Prior to irradiation, the reaction system was stirred in dark for 1 h to achieve the adsorption−desorption equilibrium between the sample and the reactant. Light absorption of the sample solution (2.5 mL) was analyzed at every 1 h interval during the reaction process on a Varian UV−visible light spectrometer (Cary-50, Varian Co.). Conversion efficiency of the reactant during the photoreduction reaction was calculated according to the formula as follows:

$$\text{Conversion}\ (\%) = [(C_0 - C)/C_0] \times 100$$

where C_0 is the original concentration of the reactant and C is the concentration of the reactant at every 1 h interval after the photocatalytic reaction.

3. RESULTS AND DISCUSSION

As illustrated in Scheme 1, well-defined NP-TNTAs was first prepared by a two-step anodization approach, which leads to hierarchically ordered structure. Subsequently, the calcined NP-TNTAs was modified with polyelectrolyte of poly(diallyldimethylammonium chloride) (PDDA) to produce a positively charged surface which is of great importance to the electrostatic attraction with tailor-made negatively charged Au NPs. Afterward, PDDA was removed through calcination and the thus-obtained calcined Au/NP-TNTAs were further treated with aminopropyl-trimethoxysilane (APS) to obtain another positively charged surface for integrating with negatively charged Au_x clusters, which gives rise to Au_x/Au/NP-TNTAs ternary heterostructure. Finally, APS was photocatalytically removed via UV light irradiation. For comparison, Au_x/NP-TNTAs binary counterpart was also prepared by analogous assembly strategy based on electrostatic interaction (Figure S12). The synthesis and characterization of Au NPs, Au_x clusters, and NP-TNTAs, which were utilized as nanobuilding blocks for LbL assembly buildup, were provided in Figure S1, Figure S2−S6, and Figure S7, respectively.

The morphologies of different samples were studied by field-emission scanning electron microscopy (FESEM). As displayed in Figure S7a, NP-TNTAs shows a characteristic hierarchically ordered pore structure. Cross-sectional FESEM images in Figure S7b−d further reveal that NP-TNTAs consists of periodic porous structure with a mean size of ca. 90 nm on the top and self-aligned nanotube arrays in the bottom with thickness of ca. 9 μm. With regard to the morphology of Au/NP-TNTAs, panoramic (Figure 1a) and side-view (Figure S8) FESEM images demonstrate that Au NPs are densely assembled on the scaffold of NP-TNTAs without agglomeration. In addition, as displayed in Figure 1c,e, morphologies of Au_x/NP-TNTAs and Au_x/Au/NP-TNTAs nanostructures are similar to those of NP-TNTAs and Au/NP-TNTAs, respectively, which is mainly ascribed to ultrasmall size of Au_x clusters (1.51 nm, Figure S2−S3), which makes direct differentiation of Au_x clusters rather difficult.

To obtain more enriched information on the microscopic structure, transmission electron microscopy (TEM) measurements were performed. As revealed by TEM images of Au/NP-TNTAs in Figure 1b and Figure S9, Au NPs are evenly distributed on the entire NP-TNTAs scaffold, indicating surface modification with PDDA is essential for LbL assembly of Au/NP-TNTAs nanostructures. Consistently, control experiments in Figure S10−S11 ascertained the vital role of PDDA for uniform deposition of Au NPs on NP-TNTAs framework. Figure 1d and Figure S13 show the TEM images of Au_x/NP-TNTAs, from which it is clear to see that large amounts of monodispersed Au_x clusters are uniformly and intimately deposited on the NP-TNTAs framework. Furthermore, uniform distribution and intimate interfacial contact of Au_x clusters and Au NPs with NP-TNTAs in the ternary system are revealed by the high-resolution (HR) TEM images (Figure 1f and Figure S14), in which a single Au NP is closely embraced by several Au_x clusters. Elemental mapping results, as shown in Figure 1g−i and Figure S15, corroborate the attachment of different Au components in NP-TNTAs scaffold. Additionally, interplanar spacings of 0.233 nm in Figure S9d and 0.352 nm in Figure 1d,f can be attributed to (111) and (101) crystal planes of face centered cubic (fcc) Au nanocrystals and anatase TiO_2, respectively. It should be mentioned that crystal lattice of Au_x clusters cannot be observed in HRTEM images because of their strikingly different electronic structure.

Figure 2 shows the X-ray diffraction (XRD) patterns of NP-TNTAs without and with calcination as well as XRD pattern of

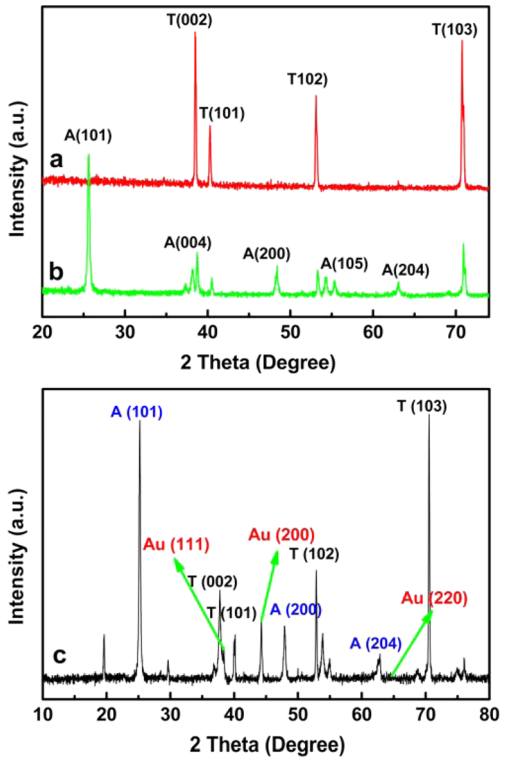

Figure 2. XRD patterns of NP-TNTAs (a) without and (b) with calcination and (c) XRD pattern of Au_x/Au/NP-TNTAs ternary heterostructure. (A: Anatase, T: Ti foil).

Au_x/Au/NP-TNTAs ternary nanostructure. As displayed in Figure 2b, the featured peaks at 2θ values of 25.3°, 37.8°, 48.0°, 53.9°, 62.7°, and 75.0° are indexed to (101), (004), (200), (105), (204), and (215) crystal planes of anatase TiO_2 (JCPDS file NO. 21−1272), which agree with the HRTEM result (Figure S14c). Moreover, as revealed in Figure 2c, apart from anatase TiO_2 diffraction peaks, the peaks at 2θ values of 38.2°, 44.4°, and 64.6° are attributable to (111), (200), and (220) crystallographic facets of Au (JCPDS file NO. 65−2870), indicating deposition of Au NPs in the ternary composite. Notably, no diffraction peak corresponding to Au_x clusters was observed, which could be attributed to low deposition amount of Au_x clusters as well as peak broadening as a result of their ultrasmall particle size.[25]

DOI: 10.1021/jacs.5b06323
J. Am. Chem. Soc. 2015, 137, 10735−10744

As shown in Figure 3A, Raman spectra exhibit four characteristic peaks at 146 (E_g), 399 (B_{1g}), 517 (A_{1g} + B_{1g})

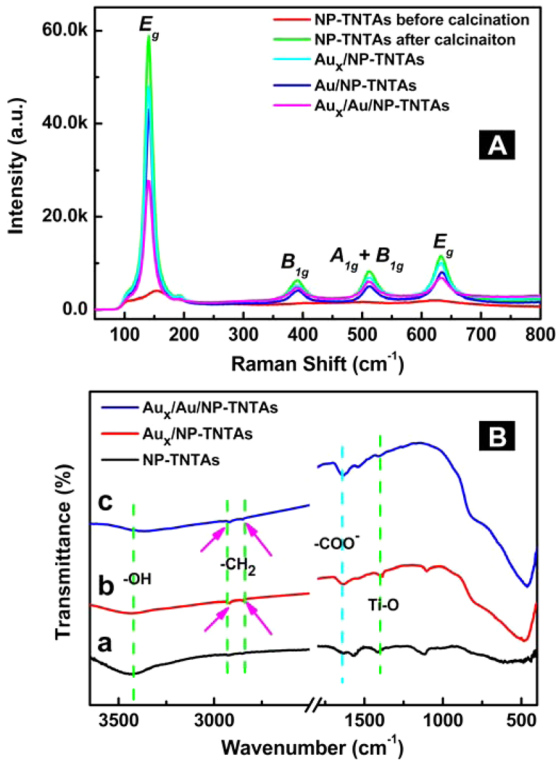

Figure 3. (A) Raman spectra of NP-TNTAs, Au/NP-TNTAs, Au$_x$/NP-TNTAs, and Au$_x$/Au/NP-TNTAs. (B) Fourier transform infrared (FTIR) spectra of (a) NP-TNTAs, (b) Au$_x$/NP-TNTAs, and (c) Au$_x$/Au/NP-TNTAs.

and 639 cm^{-1} (E_g) for all samples except for NP-TNTAs before calcination, which can be assigned to anatase TiO_2. Similarly, no typical peak corresponding to Au$_x$ clusters was observed. Moreover, all Raman peak intensities especially those corresponding to E_g modes decrease with deposition of Au$_x$ clusters and Au NPs, indicating synergistic inteaction of Au$_x$ clusters and Au NPs with NP-TNTAs.

With regard to Fourier transform infrared (FTIR) spectrum of Au$_x$/Au/NP-TNTAs (Figure 3Bc), besides typical TiO_2 peaks located at 3443.9 cm^{-1} (−OH), 1415.0 and 1115.0 cm^{-1} (Ti−O), (Figure 3Ba),[32] another two peaks at 2918.4 and 2850.5 cm^{-1} and one peak at 1628 cm^{-1} appear, which correspond to stretching vibration modes of $-CH_2$ and −COOH groups from GSH ligand, corroborating successful anchoring of Au$_x$ clusters in the ternary composite. The observation is also consistent with the FTIR result of Au$_x$/NP-TNTAs (Figure 3Bb). Furthermore, it is revealed that all TiO_2 peaks in Au$_x$/Au/NP-TNTAs are blue-shifted as compared with NP-TNTAs, once again suggesting pronounced interaction of Au$_x$ clusters and Au NPs with NP-TNTAs.

Compositional information and elemental chemical states of different samples were disclosed by X-ray photoelectron spectroscopy (XPS). Survey spectrum of Au$_x$/Au/NP-TNTAs (Figure 4a) confirms the coexistence of Ti, O, and Au in the ternary composite. It should be emphasized that no Si and N signals were detected in the survey spectrum, indicating that PDDA and APS were completely removed by calcination and UV light irradiation. High-resolution XPS spectra of O 1s (Figure 4b) and Ti 2p (Figure 4c) verified the phase preservation of NP-TNTAs during the LbL assembly buildup. Additionally, as displayed in Figure 4d, high-resolution Au spectrum reveals two doublet 4f peaks, which indicates the existence of Au species with two different chemical states in the ternary heterostructure. The Au $4f_{5/2}$ and Au $4f_{7/2}$ peaks with binding energy (BE) of 87.4 and 83.8 eV are attributable to Au^0 from internal layer of Au$_x$ clusters and Au NPs, which is also reflected in the high-resolution Au 4f spectrum of Au/NP-TNTAs (Figure 4e).[33,34] The other doublet located at 88.5 and 84.9 eV are assigned to Au^+ from surface layer of clusters.[35] Consequently, XPS results strongly corroborate the deposition of core−shell Au$_x$ clusters, i.e., Au(0)@Au(I)-GSH, and Au NPs in ternary composite via LbL self-assembly approach.[19,21] XPS result of blank NP-TNTAs is displayed in Figure S16 for comparison and chemical bond species versus BE for NP-TNTAs and Au$_x$/Au/NP-TNTAs are summarized in Table S1.

UV−vis diffuse reflectance spectra (DRS) were collected to determine the optical properties. As displayed in Figure 5a, Au$_x$/Au/NP-TNTAs exhibits remarkably enhanced light absorption in comparison with Au$_x$/NP-TNTAs and NP-TNTAs with a redshift of band edge to the visible region (Figure 5b). Besides, a substantial surface plasmon resonance (SPR) absorption peak at ca. 530 nm can be apparently observed. This indicates that concurrent deposition of Au$_x$ clusters and Au NPs on NP-TNTAs can improve the light absorption of NP-TNTAs in the visible region. It should be noted that the light absorption beyond 500 nm for NP-TNTAs arises from light trapping due to the hierarchical structure. This conclusion could be confirmed by comparing the DRS results of NP-TNTAs, TNTAs (Figure S17a), and TiO_2 particulate film (Figure S17b).

Photocatalytic performances were probed by anaerobic reduction of aromatic nitro compounds to corresponding amino compounds, e.g., 4-nitroaniline (4-NA) to 4-phenylenediamine (4-PDA) under visible light (λ > 420 nm) irradiation.[36] Blank experiments indicate that the reaction is driven by a photocatalytic process (Figure S18). As shown in Figure 6a, Au$_x$/Au/NP-TNTAs ternary nanostructure demonstrates significantly enhanced photoactivity in comparison with NP-TNTAs and binary counterparts toward photoreduction of 4-NA under visible light (λ > 420 nm) irradiation. Additionally, similar results have also been observed for photoreduction of 2-NA and 3-NA (Figure 6b,c) as well as 4(3 or 2)-nitrophenol (NP) (Figure 6d−f) under the same experimental conditions. Photocatalytic performances of different samples toward reduction of aromatic nitro compounds follow the orders of Au$_x$/Au/NP-TNTAs > Au$_x$/NP-TNTAs > Au/NP-TNTAs > NP-TNTAs, with corresponding reaction rate constants summarized in Table S2. It is noteworthy that the role of plasmon excitation of Au NPs was evidently mirrored by the substantially improved photoactivity of Au/NP-TNTAs in comparison with NP-TNTAs. Furthermore, with a view to determining the active spectrum region that contributes to the enhanced photoactivities of Au$_x$/Au/NP-TNTAs ternary composite, action spectrum under monochromatic light irradiation was collected. As revealed in Figure 7, action spectrum of Au$_x$/Au/NP-TNTAs matches well with the corresponding DRS result, thereby evidencing the synergistic contribution from plasmon excitation of Au NPs and photosensitization effect of Au$_x$ clusters. Furthermore, to highlight the pivotal role of photogenerated electrons in the photoreduction process, control experiments before and after

DOI: 10.1021/jacs.5b06323
J. Am. Chem. Soc. 2015, 137, 10735−10744

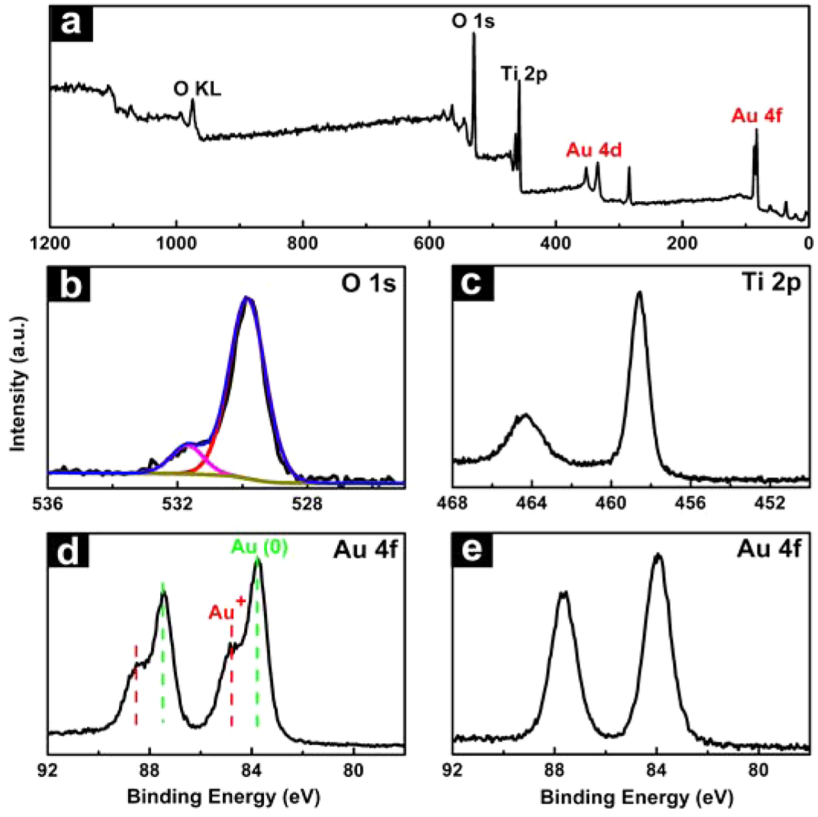

Figure 4. (a) Survey spectrum and high-resolution XPS spectra of (b) O 1s and (c) Ti 2p, (d) Au 4f for Au_x/Au/NP-TNTAs, and (e) high-resolution Au 4f spectrum of Au/NP-TNTAs.

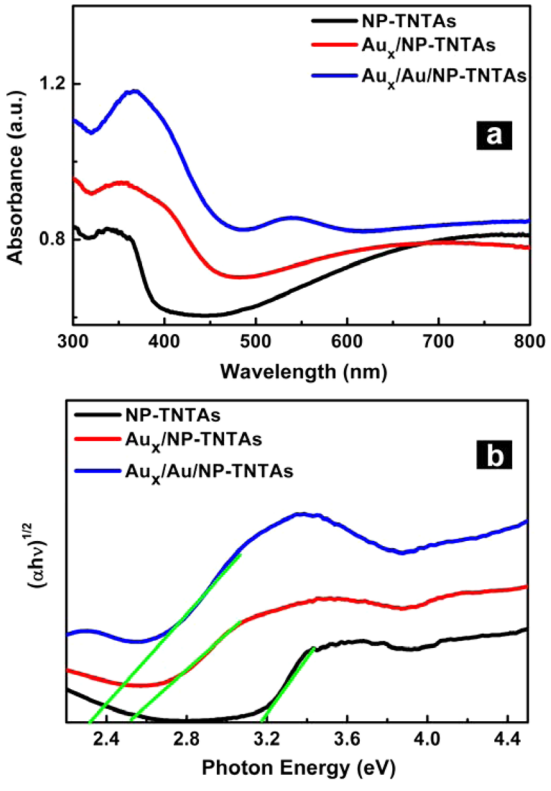

Figure 5. (a) UV–vis diffuse reflectance spectra (DRS) of NP-TNTAs, Au_x/NP-TNTAs, and Au_x/Au/NP-TNTAs, and (b) plots of transformed Kubelka–Munk function versus the energy of light.

the involvement of $K_2S_2O_8$, which was used as a photoelectron quencher in N_2 atmosphere, were performed (Figure S19), for which photoreduction of 4-NA over Au_x/Au/NP-TNTAs was completely suppressed with the introduction of $K_2S_2O_8$, therefore highlighting the crucial role of photoexcited electrons in triggering the photoreduction reactions. Structural advantage of well-defined NP-TNTAs over TiO_2 particulate thin film to promote photocatalytic and PEC performances was ascertained, as shown in Figure S20b,d, which could be attributed to efficient charge transport in NP-TNTAs. Furthermore, the influence of assembly order of building blocks was also probed, which emphasizes the importance of deposition fashion of Au NPs and Au_x clusters in boosting photocatalytic performances of ternary nanocomposites (Figure S20a,c).

Photoelectrochemical (PEC) measurements were further performed to explore the role of interfacial integration between Au ingredients and NP-TNTAs and, meanwhile, to probe the separation of photoinduced electron–hole charge carriers in the reaction system. Figure 8a shows the transient photocurrent responses of different samples under chopped visible light illumination (λ > 420 nm). It is clear to see that concurrent deposition of Au NPs and Au_x clusters via LbL assembly strategy is conducive to remarkably enhancing photocurrent of NP-TNTAs under visible light irradiation, which follows the same order to the photocatalytic performance: Au_x/Au/NP-TNTAs > Au_x/NP-TNTAs > Au/NP-TNTAs > NP-TNTAs. The significantly improved photocurrent indicates a more effective separation and longer lifetime of photogenerated electron–hole pairs over Au_x/Au/NP-TNTAs ternary nanostructure as compared with binary and single counterparts. Consistently, as shown in Figure 8b, LSV results (dark current is zero) exhibit analogous trends, thus confirming synergistic

DOI: 10.1021/jacs.5b06323
J. Am. Chem. Soc. 2015, 137, 10735–10744

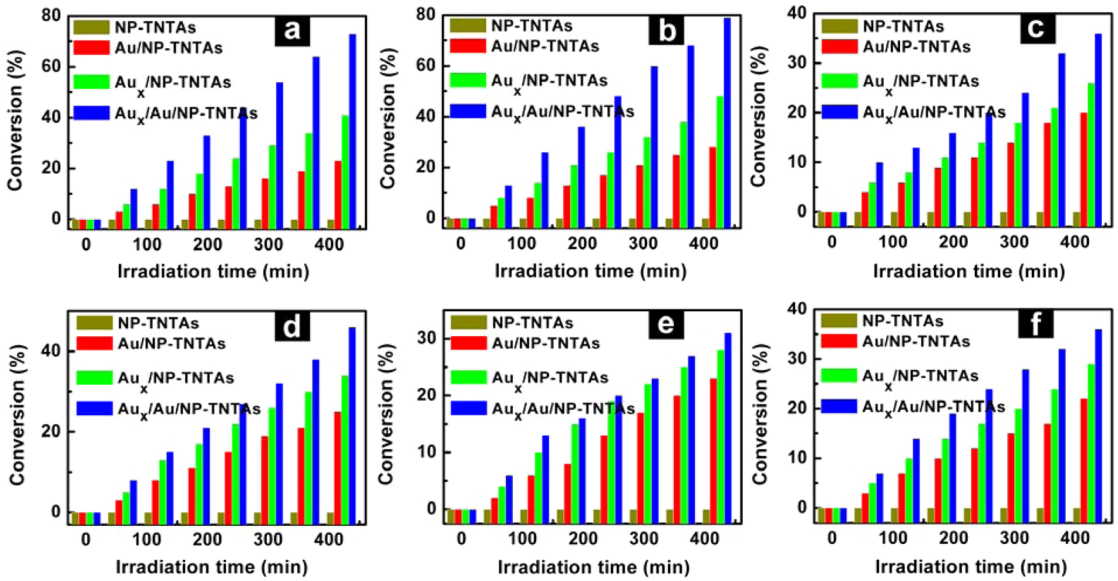

Figure 6. Photocatalytic reduction of (a) 4-NA, (b) 2-NA, (c) 3-NA, (d) 4-nirtrophenol (4-NP), (e) 2-NP, and (f) 3-NP over NP-TNTAs, Au/NP-TNTAs (two assembly cycles), Au_x/NP-TNTAs (dipping time of 125 h), and Au_x/Au/NP-TNTAs (Au: two assembly cycles, Au_x: dipping time of 125 h) heterostructures under visible light irradiation (λ > 420 nm), in which ammonium formate was added as scavenger for photoinduced holes in combination with N_2 purge under ambient conditions.

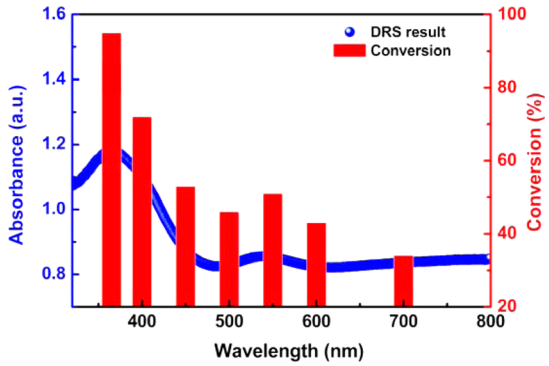

Figure 7. Action spectrum for photoreduction of 4-NA over Au_x/Au/NP-TNTAs (Au: two assembly cycles, Au_x: dipping time of 125 h).

contribution of Au NPs and Au_x clusters for photocurrent generation. Notably, photocurrent of Au_x/Au/NP-TNTAs under continuous visible light irradiation (Figure 8e) indicates the favorable photostability.

Electrochemical impedance spectroscopy (EIS) was further applied to evaluate the separation efficiency of photogenerated charge carriers.[37] As displayed in Figure S21, EIS Nyquist plots of Au_x/Au/NP-TNTAs and Au_x/NP-TNTAs exhibit substantially smaller semicircles in comparison with Au/NP-TNTAs and NP-TNTAs, implying much more efficient interfacial electron transfer imparted by Au_x clusters. Furthermore, EIS results in low-frequency region (Figure 8c) reflect smaller semicircle of Au_x/Au/NP-TNTAs than Au_x/NP-TNTAs, suggesting that intimate integration of Au NPs within the interface of Au_x clusters and NP-TNTAs could further reduce the charge transport resistance. Lifetime of photoelectrons was estimated from open circuit photovoltage decay measurements by turning off illumination at steady state and monitoring the subsequent decay of photovoltage with time.[38] As shown in Figure 8d, Au_x/Au/NP-TNTAs exhibits prolonged electron lifetime as compared with single and binary counterparts, which should be responsible for the enhanced PEC performances.

Incident photon-to-current conversion efficiency (IPCE) measurements were performed to reveal the underlying reasons for the generation of photocurrent versus incident light wavelength. As shown in Figure S22a, blank NP-TNTAs only exhibits substantial IPCE in the UV region which agrees with the wide bandgap nature of TiO_2, indicating that the hierarchically ordered structure of NP-TNTAs could not contribute to photocurrent generation in the visible spectrum. This result is consistent with the observed negligible transient photocurrent response of NP-TNTAs under visible light irradiation (λ > 420 nm) (Figure 8a,b). Figure S22b shows the IPCE of Au/NP-TNTAs nanostructure, which demonstrates almost the same shape to that of NP-TNTAs except the appearance of a pronounced peak at about 530 nm, thereby indicating the important role played by Au NPs to generate photocurrent under visible light irradiation through surface plasmon effect. The IPCE curve of Au_x/NP-TNTAs (Figure S22c) is similar to that of NP-TNTAs other than the absorption edge was red-shifted to visible region, which is in line with the light absorption of Au_x clusters (Figure S4), corroborating the imperative role of Au_x clusters in improving the photocurrent of Au_x/NP-TNTAs in the visible region. Additionally, it is clear to see from Figure S22d that IPCE spectrum of Au_x/Au/NP-TNTAs exhibits a substantial redshift to the visible region in conjunction with a SPR peak, suggesting the synergistic contributions of Au NPs and Au_x clusters in boosting the photocurrent of ternary heterostructure under visible light irradiation. For clear comparison, IPCE results of different samples in the visible region were enlarged and combined in Figure 8f.

Besides, PEC performances of Au/NP-TNTAs nanostructures with varied assembly cycles of Au NPs were also probed (Figure S23–S25), based on which optimal assembly cycle was determined to be two cycles. Similarly, optimal dipping time of Au_x clusters for Au_x/Au/NP-TNTAs ternary heterostructure (two assembly cycles of Au NPs) under visible light irradiation was determined to be 125 h (Figure S26–S28). Therefore,

DOI: 10.1021/jacs.5b06323
J. Am. Chem. Soc. 2015, 137, 10735–10744

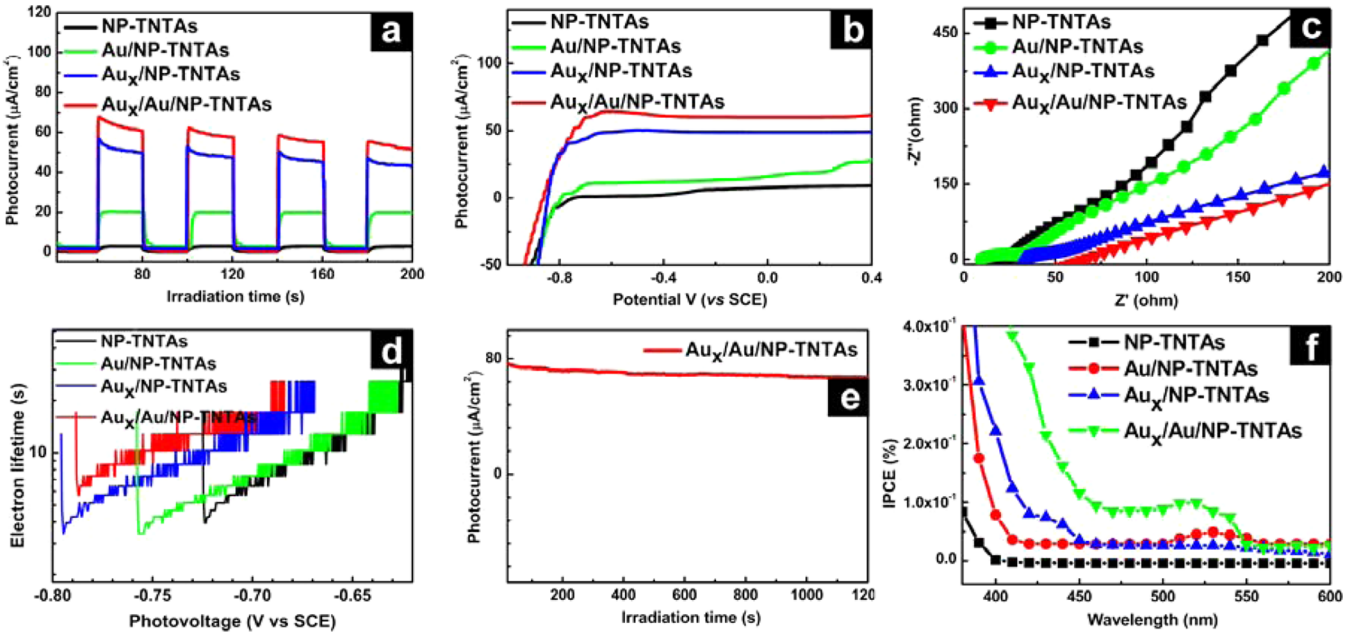

Figure 8. (a) Transient photocurrent responses, (b) linear-sweep voltammograms (LSV, scan rate: 5 mV/s), (c) electrochemical impedance spectroscopy (EIS) Nyquist plots in low-frequency region, (d) electron lifetime, and (f) IPCE spectra of NP-TNTAs, Au/NP-TNTAs (two assembly cycles), Au$_x$/NP-TNTAs (dipping time of 125 h), and Au$_x$/Au/NP-TNTAs (Au: two assembly cycles, Au$_x$: dipping time of 125 h) heterostructures in a 0.1 M Na_2S aqueous solution under visible light irradiation (λ > 420 nm). (e) Photostability of Au$_x$/Au/NP-TNTAs.

PEC performances of Au$_x$/Au/NP-TNTAs could be tuned by assembly cycle and dipping time during LbL assembly process.

To reveal the underlying reasons for the significantly enhanced PEC and photocatalytic performances of Au$_x$/Au/NP-TNTAs, photoluminescence (PL) measurements monitoring the fate of electron−hole pairs were carried out.[39] Figure 9a shows that PL intensity of Au$_x$ clusters aqueous solution was greatly quenched with the addition of TiO_2 and further quenched by adding Au NPs, thus strongly supporting the injection of photoexcited electrons from Au$_x$ clusters to the conduction band (CB) of TiO_2 via electron relay of Au NPs, leading to improved separation of photogenerated electron−hole pairs. Hence, PL results indicate that the lifespan of electron−hole pairs produced over Au$_x$ clusters can be tuned by Au NPs based on synergistic interaction. PL result of NP-TNTAs was also probed to attain more enriched information on the correlation between NP-TNTAs and Au ingredients in tuning the photogenerated electrons. As displayed in Figure 9b and Figure S29, PL intensity of NP-TNTAs arising from photoexcitation of defects level in TiO_2[40] was reduced gradually with the deposition of Au NPs, Au$_x$ clusters, and concurrent Au$_x$ clusters and Au NPs and it follows the order of Au$_x$/Au/NP-TNTAs < Au$_x$/NP-TNTAs < Au/NP-TNTAs < NP-TNTAs, in combination with a redshift of peak. From which, it was speculated that photoexcited electrons from oxygen vacancy level of TiO_2 could be captured by Au$_x$ clusters and Au NPs, in which metallic Au^0 core of Au$_x$ clusters and Au NPs serve as "electron trap" to capture the photogenerated electrons, thereby evidently corroborating the capability of metallic Au component in composite as electron relay mediator in current reaction system.

Photocatalytic and PEC mechanisms of Au$_x$/Au/NP-TNTAs ternary system under visible light irradiation were displayed in Figure S30 and Figure S31, respectively. Specifically, it has been well-established that Au$_x$ clusters with distinct Highest Occupied Molecular Orbital (HOMO)-Lowest Unoccupied

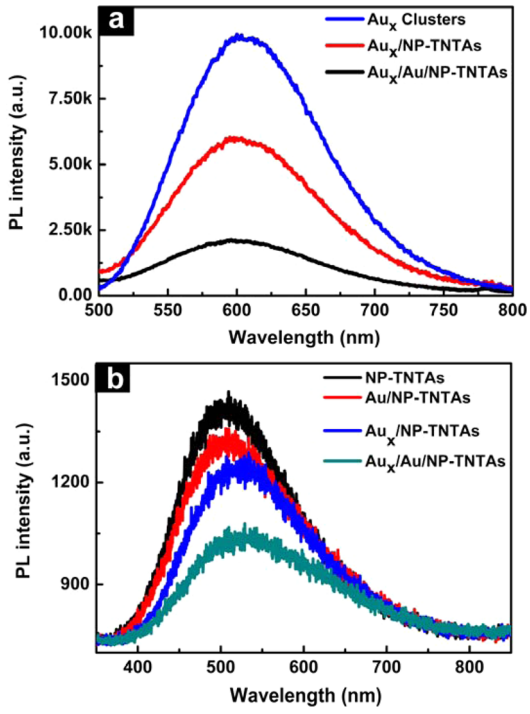

Figure 9. (a) Emission spectra of Au$_x$ clusters aqueous solution with the addition of TiO_2 scratched from NP-TNTAs scaffold and Au NPs aqueous solution, for which excitation wavelength was set at 425 nm. (b) Photoluminescence (PL) results of NP-TNTAs, Au/NP-TNTAs, Au$_x$/NP-TNTAs, and Au$_x$/Au/NP-TNTAs with excitation wavelength set at 500 nm.

Molecular Orbital (LUMO) gap is able to act like a semiconductor with small bandgap.[25,41] Accordingly, in current reaction system, electrons can be photoexcited from HOMO to LUMO over Au$_x$ clusters under visible light irradiation to produce electron−hole pairs. Moreover, according to PL

DOI: 10.1021/jacs.5b06323
J. Am. Chem. Soc. 2015, 137, 10735−10744

Scheme 2. Electron Transfer Pathways in Au_x/Au/NP-TNTAs Ternary System[a]

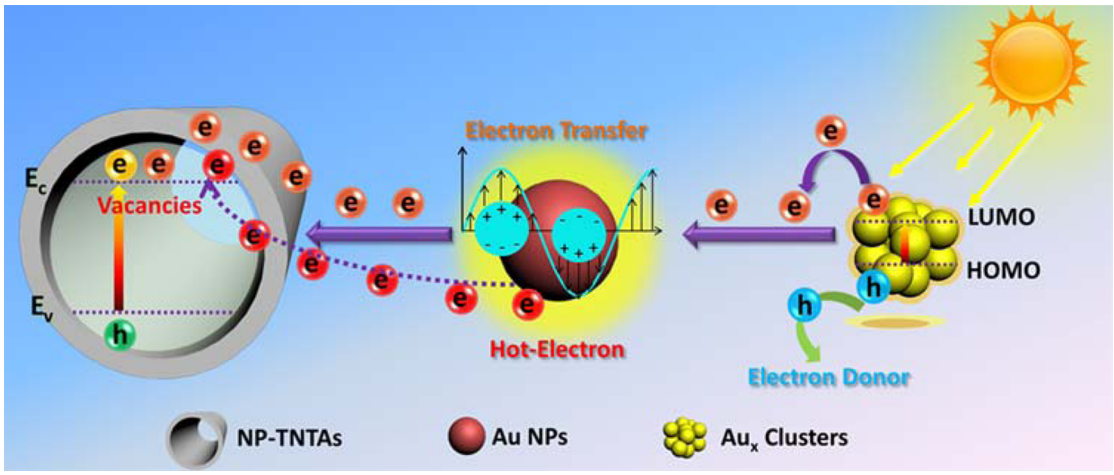

[a]Orange electrons: electrons photoexcited from Au_x clusters; Red electrons: hot electrons produced from plasmon excitation of Au NPs.

analysis and previous studies,[25,41] LUMO level of Au_x clusters has been determined to locate above the CB of TiO_2 and Femi level of Au. In this regard, as depicted in Scheme 2, there exist two main transfer pathways for electrons photoexcited over Au_x clusters. The first is the direct transfer of photoexcited electrons from Au_x clusters to the CB of TiO_2 based on suitable band alignment between clusters and TiO_2; the other involves the first transfer of electrons from clusters to the Femi level of Au NPs and then to the CB of TiO_2 in which Au NPs act as a bridging medium to reinforce the flow of electrons.

On the other hand, it is worthwhile to know that "hot electrons" generated from plasmon excitation of Au NPs under visible light irradiation could also flow to the CB of TiO_2, therefore increasing the density of photogenerated electrons in reaction system. Additionally, localized oscillating electric field afforded by plasmonic absorption of Au NPs may also facilitate the transport of electrons photogenerated over Au_x clusters.[42,43] Meanwhile, photogenerated holes produced on the HOMO of Au_x clusters and "hot holes" over Au NPs are rapidly quenched by hole scavengers, leading to separation of charge carriers. In this way, these in situ photoinduced electrons from Au_x clusters and plasmonic Au NPs concurrently reduce the aromatic nitro compounds or directly transfer to the external circuit to produce photocurrent, resulting in significantly enhanced photoreduction and PEC performances of Au_x/Au/NP-TNTAs ternary heterostructure.

4. CONCLUSION

In summary, well-defined Au NPs and Au_x clusters coadorning NP-TNTAs ternary heterostructure as a novel light-harvesting antenna has been rationally designed by a facile LbL self-assembly strategy based on pronounced electrostatic interaction, by which nanobuilding blocks were judiciously and intimately integrated in a tunable fashion. Moreover, it was found that these hierarchically ordered Au_x/Au/NP-TNTAs ternary nanocomposites exhibit significantly improved PEC and photocatalytic performances under visible light irradiation at ambient conditions as compared with single and binary counterparts. More significantly, the imperative roles of Au NPs as electron relay mediator and plasmonic sensitizer for Au_x clusters during the photocatalytic and PEC processes were for the first time ascertained. Finally, PEC and photocatalytic mechanisms were presented. It is believed that our work could open up new avenues for the rational design of metal cluster/metal nanocrystal/semiconductor nanocomposites and, more importantly, to bridge the gap between metal clusters and metal nanocrystals for versatile photocatalytic, PEC, and photovoltaic applications.

■ ASSOCIATED CONTENT

Supporting Information

The Supporting Information is available free of charge on the ACS Publications website at DOI: 10.1021/jacs.5b06323.

Characterizations of building blocks for LbL assembly buildup including Au NPs, Au_x clusters, and NP-TNTAs substrate. Characterizations of binary and ternary heterostructure counterparts including Au/NP-TNTAs, Au_x/NP-TNTAs, and Au_x/Au/NP-TNTAs. Model of GSH-capped Au_x clusters. High-resolution XPS spectra of N 1s with and without calcination for Au/NP-TNTAs. Morphologies of Au/NP-TNTAs prepared with and without the modification of PDDA. Blank experiments for photocatalytic reduction reaction. Photocatalytic reaction rate constants toward photoreduction reactions. Photocatalytic performance of Au_x/Au/NP-TNTAs with addition of $K_2S_2O_8$ as photogenerated electron scavenger. Photoreduction and PEC activities of Au/Au_x/NP-TNTAs and Au_x/Au/TiO_2 particulate film in comparison with Au_x/Au/NP-TNTAs. Individual IPCE result of different samples. Characterization and PEC activities of Au/NP-TNTAs nanostructures with different assembly cycles of Au NPs. Characterization and PEC performances of Au_x/Au/NP-TNTAs ternary nanostructures with different dipping time in Au_x cluster aqueous solution. Schematic illustration depicting the photocatalytic and PEC mechanisms of Au_x/Au/NP-TNTAs ternary nanocomposite. (PDF)

■ AUTHOR INFORMATION

Corresponding Author

*liubin@ntu.edu.sg

Notes

The authors declare no competing financial interest.

DOI: 10.1021/jacs.5b06323
J. Am. Chem. Soc. 2015, 137, 10735−10744

■ ACKNOWLEDGMENTS

This work was supported by the Nanyang Technological University startup grant: M4080977.120, Singapore Ministry of Education Academic Research Fund (AcRF) Tier 1: M4011021.120 and Public Sector Funding from Agency for Science, Technology and Research of Singapore (A*Star): M4070232.120.

■ REFERENCES

(1) Leschkies, K. S.; Divakar, R.; Basu, J.; Enache-Pommer, E.; Boercker, J. E.; Carter, C. B.; Kortshagen, U. R.; Norris, D. J.; Aydil, E. S. *Nano Lett.* **2007**, *7*, 1793.
(2) Xiao, F.-X.; Miao, J.; Tao, H. B.; Hung, S.-F.; Wang, H.-Y.; Yang, H. B.; Chen, J.; Chen, R.; Liu, B. *Small* **2015**, *11*, 2115.
(3) Liu, C.; Dasgupta, N. P.; Yang, P. *Chem. Mater.* **2014**, *26*, 415.
(4) Law, M.; Goldberger, J.; Yang, P. *Annu. Rev. Mater. Res.* **2004**, *34*, 83.
(5) Xu, Y.-J.; Zhuang, Y.; Fu, X. *J. Phys. Chem. C* **2010**, *114*, 2669.
(6) Liu, B.; Chen, H. M.; Liu, C.; Andrews, S. C.; Hahn, C.; Yang, P. *J. Am. Chem. Soc.* **2013**, *135*, 9995.
(7) Liu, B.; Liu, L.-M.; Lang, X.-F.; Wang, H.-Y.; Lou, X. W.; Aydil, E. S. *Energy Environ. Sci.* **2014**, *7*, 2592.
(8) Li, J.; Zeng, H. C. *Angew. Chem., Int. Ed.* **2005**, *44*, 4416.
(9) Bian, Z.; Tachikawa, T.; Zhang, P.; Fujitsuka, M.; Majima, T. *J. Am. Chem. Soc.* **2014**, *136*, 458.
(10) Li, J.; Cushing, S. K.; Zheng, P.; Senty, T.; Meng, F.; Bristow, A. D.; Manivannan, A.; Wu, N. *J. Am. Chem. Soc.* **2014**, *136*, 8438.
(11) Xiao, F.-X.; Miao, J.; Liu, B. *Mater. Horiz.* **2014**, *1*, 259.
(12) Luo, Z. T.; Yuan, X.; Yu, Y.; Zhang, Q. B.; Leong, D. T.; Lee, J. Y.; Xie, J. *J. Am. Chem. Soc.* **2012**, *134*, 16662.
(13) Schuller, J. A.; Barnard, E. S.; Cai, W.; Jun, Y. C.; White, J. S.; Brongersma, M. L. *Nat. Mater.* **2010**, *9*, 193.
(14) Tian, Y.; Tatsuma, T. *J. Am. Chem. Soc.* **2005**, *127*, 7632.
(15) Chen, H. J.; Shao, L.; Li, Q.; Wang, J. F. *Chem. Soc. Rev.* **2013**, *42*, 2679.
(16) Qian, K.; Sweeny, B. C.; Johnston-Peck, A. C.; Niu, W.; Graham, J. O.; DuChene, J. S.; Qiu, J.; Wang, Y.-C.; Engelhard, M. H.; Su, D.; Stach, E. A.; Wei, W. D. *J. Am. Chem. Soc.* **2014**, *136*, 9842.
(17) Katagi, Y.; Kazuma, E.; Tatsuma, T. *Nanoscale* **2014**, *6*, 14543.
(18) Schuller, J. A.; Barnard, E. S.; Cai, W.; Jun, Y. C.; White, J. S.; Brongersma, M. L. *Nat. Mater.* **2010**, *9*, 193.
(19) Chen, Y.-S.; Choi, H. B.; Kamat, P. V. *J. Am. Chem. Soc.* **2013**, *135*, 8822.
(20) Chen, Y.-S.; Kamat, P. V. *J. Am. Chem. Soc.* **2014**, *136*, 6075.
(21) Stamplecoskie, K. G.; Kamat, P. V. *J. Phys. Chem. Lett.* **2015**, *6*, 1870.
(22) Wang, Y.; Su, H.; Xu, C.; Li, G.; Gell, L.; Lin, S.; Tang, Z.; Hakkinen, H.; Zheng, N. *J. Am. Chem. Soc.* **2015**, *137*, 4324.
(23) Yang, H.; Wang, Y.; Yan, J.; Chen, X.; Zhang, X.; Hakinen, H.; Zheng, N. *J. Am. Chem. Soc.* **2014**, *136*, 7197.
(24) Li, G.; Jin, R. *Acc. Chem. Res.* **2013**, *46*, 1749.
(25) Yu, C. L.; Li, G.; Kumar, S.; Kawasaki, H.; Jin, R. *J. Phys. Chem. Lett.* **2013**, *4*, 2847.
(26) Chen, H. M.; Chen, C. K.; Liu, R.-S.; Zhang, L.; Zhang, J.; Wilkinson, D. P. *Chem. Soc. Rev.* **2012**, *41*, 5654.
(27) Decher, G. *Science* **1997**, *277*, 1232.
(28) Caruso, F.; Caruso, R. A.; Mohwald, H. *Science* **1998**, *282*, 1111.
(29) Cho, J.; Quinn, J. F.; Caruso, F. *J. Am. Chem. Soc.* **2004**, *126*, 2270.
(30) Xiao, F.-X.; Miao, J.; Liu, B. *J. Am. Chem. Soc.* **2014**, *136*, 1559.
(31) Dotzauer, D. M.; Dai, J. H.; Sun, L.; Bruening, M. L. *Nano Lett.* **2006**, *6*, 2268.
(32) Kumar, P. M.; Badrinarayanan, S.; Sastry, M. *Thin Solid Films* **2000**, *358*, 122.
(33) Fang, C.; Jia, H.; Chang, S.; Ruan, Q.; Wang, P.; Chen, T.; Wang, J. *Energy Environ. Sci.* **2014**, *7*, 3431.
(34) Xiao, F. *J. Phys. Chem. C* **2012**, *116*, 16487.
(35) Huang, J.; Dai, W. L.; Fan, K. N. *J. Catal.* **2009**, *266*, 228.
(36) Zhang, N.; Xu, Y.-J. *Chem. Mater.* **2013**, *25*, 1979.
(37) Li, N.; Liu, G.; Zhen, C.; Li, F.; Zhang, L. L.; Cheng, H. M. *Adv. Funct. Mater.* **2011**, *21*, 1717.
(38) Meekins, B. H.; Kamat, P. V. *ACS Nano* **2009**, *3*, 3437.
(39) Zhang, Y.; Zhang, N.; Tang, Z.-R.; Xu, Y.-J. *ACS Nano* **2012**, *6*, 9777.
(40) Mercado, C. C.; Knorr, F. J.; McHale, J. L. *ACS Nano* **2012**, *6*, 7270.
(41) Xiao, F.-X.; Hung, H.-F.; Miao, J.; Wang, H.-Y.; Yang, H.; Liu, B. *Small* **2015**, *1*, 554.
(42) Jiang, R. B.; Li, B. X.; Fang, C. H.; Wang, J. *Adv. Mater.* **2014**, *26*, 5274.
(43) Xiao, M. D.; Jiang, R. B.; Wang, F.; Fang, C. H.; Wang, J.; Yu, J. C. *J. Mater. Chem. A* **2013**, *1*, 5790.

DOI: 10.1021/jacs.5b06323
J. Am. Chem. Soc. 2015, 137, 10735−10744